

# Modeling and Computational Fluid Dynamics—Population Balance Equation—Micromixing Simulation of Impinging Jet Crystallizers

Xing Yi Woo,<sup>†,‡</sup> Reginald B. H. Tan,<sup>\*,‡,§</sup> and Richard D. Braatz<sup>\*,†</sup>

Department of Chemical and Biomolecular Engineering, University of Illinois at Urbana-Champaign, 600 South Mathews Avenue, Urbana, Illinois 61801, Department of Chemical and Biomolecular Engineering, National University of Singapore, 4 Engineering Drive 4, Singapore 117576, and Crystallization and Particle Science Group, Institute of Chemical and Engineering Sciences, 1 Pesek Road, Jurong Island, Singapore 627833

Received January 27, 2008; Revised Manuscript Received August 11, 2008

**ABSTRACT:** Computational fluid dynamics (CFD), micromixing modeling, and the population balance equation (PBE) are coupled to simulate the crystal size distribution in a confined impinging jet crystallizer. For the antisolvent crystallization of lovastatin in confined impinging jets, the simulation results show varying degrees of inhomogeneity in the supersaturation and the nucleation and growth rates in the impinging jet crystallizer for different jet Reynolds numbers. The shape of the crystal size distribution and its variation with jet Reynolds number are consistent with experimental observations of unconfined impinging jets. The crystallization of L-histidine was also modeled to predict the crystal size distribution of stable and metastable polymorphs obtained from a confined impinging jet crystallizer. It is predicted how to adjust the inlet velocity to tailor the crystal size distribution, while the polymorph ratio remained relatively constant. The simulation results presented in this manuscript demonstrate the possibility of designing impinging jet crystallizers by modeling and simulation, to provide increased process understanding and reduce the experimental material required for design.

## 1. Introduction

Impinging jet crystallization, developed by Midler et al.<sup>1</sup> more than a decade ago, is recognized as one of the most reliable approaches to produce small crystals with a narrow size distribution. The basic principle in this design is to utilize high intensity micromixing of fluids to achieve a homogeneous composition of high supersaturation before the onset of nucleation. As highlighted by D'Aquino,<sup>2</sup> this technology is now being used by various pharmaceutical companies in their commercial drug production.<sup>3–5</sup> The direct production of small uniform crystals of high surface area that meet the bioavailability and dissolution requirements can eliminate the need for milling, which can produce dust issues, yield losses, long production times, polymorphic transformation, and amorphization.<sup>6–9</sup> A narrow particle size distribution is especially important for inhalation drugs, in which the specific size range depends on the region of the human respiratory tract where the drug is targeted.<sup>10–12</sup> Continuous crystallization using T-mixers and Y-mixers to produce small uniform particles also have been experimentally and numerically studied.<sup>13–17</sup>

Numerous experimental studies have been carried out to gain a deeper understanding of the impinging jet crystallization process so as to increase efficiency during process development and optimization. For the antisolvent crystallization of lovastatin, Mahajan and Kirwan<sup>18</sup> measured the dependency of the crystal size distribution (CSD) on the jet velocity and level of supersaturation in the impinging jet crystallizer operated in non-submerged mode. Hacherl et al.<sup>19</sup> investigated the effects of jet velocity on the crystal size distribution and the proportion of hydrates formed for the reactive crystallization of calcium oxalate. Johnson and Prud'homme<sup>20</sup> experimentally investigated

the dependency of the crystal size distribution on the jet velocity and the inlet concentrations for a confined and submerged impinging jet crystallizer in which amphiphilic diblock copolymers were added to inhibit crystal growth. Recently, Marchisio et al. applied confined impinging jets to reactive precipitation, and reported on the dependence of particle size distribution with jet velocity and inlet reactant concentrations.<sup>21</sup>

The mixing in impinging jets has been characterized by an overall micromixing time by Mahajan and Kirwan<sup>18</sup> and Johnson and Prud'homme<sup>22</sup> using competitive reactions. The micromixing times, correlated to the jet velocity, the fluid properties, and some geometrical aspects of the impinging jet crystallizer, can be used to establish scale-up criteria for impinging jets. The three-dimensional turbulent flow field in the impinging jet chamber also can be visualized experimentally (for example, by using laser-induced fluorescence, laser doppler anemometry, or particle image velocimetry) or simulated using computational fluid dynamics (CFD).<sup>23–26</sup> The modeling of mixing and reactions in impinging jets has been widely studied as well.<sup>27–31</sup> The extension of experimental visualization and simulations that include the crystal nucleation and growth would offer a deeper understanding of impinging jet crystallization, which could speed up the design of impinging jets and reduce the time required to identify the operating conditions that produce the desired crystal size distribution. Consequently, the time required to bring a new drug to the market could be reduced.

In this paper, a coupled CFD—micromixing—population balance algorithm<sup>32</sup> is used to model the crystallization process in an impinging jet crystallizer. The geometry of the confined impinging jet is adapted from Johnson and Prud'homme.<sup>22</sup> The CFD simulations of confined impinging jets of similar geometry have been reported recently by Liu and Fox,<sup>30</sup> Marchisio et al.,<sup>21</sup> and Gavi et al.<sup>31</sup> Liu and Fox<sup>30</sup> and Gavi et al.<sup>31</sup> modeled the turbulent macromixing using the  $k-\epsilon$  turbulent model with enhanced wall treatment and the micromixing using the two-environment direct quadrature method of moments (DQMOM)—interaction by exchange with the mean (IEM) model<sup>33</sup> with the

\* Corresponding author. (R.D.B.) E-mail: braatz@uiuc.edu; phone: 217-333-5073; fax: 217-333-5052. (R.B.H.T.) E-mail: chetanbh@nus.edu.sg; phone: 65-65166360; fax: 65-67791936.

<sup>†</sup> University of Illinois at Urbana-Champaign.

<sup>‡</sup> National University of Singapore.

<sup>§</sup> Institute of Chemical and Engineering Sciences.

micromixing parameter as a function of local turbulent Reynolds number. They reported good agreement with the experimental results (conversion of the slower reaction in competitive-parallel reactions at the outlet of the confined impinging jets) reported in Johnson and Prud'homme<sup>22</sup> for a wide range of jet Reynolds numbers. These studies motivate our use of the turbulent/micromixing model of Liu and Fox<sup>30</sup> and Gavi et al.<sup>31</sup> to model the antisolvent crystallization process in confined impinging jets.

In the first part, the full crystal size distribution for the antisolvent crystallization of lovastatin in the confined impinging jet crystallizer was simulated by coupling the macromixing and micromixing models with the solution of the population balance equation as described by Woo et al.,<sup>32</sup> and the effects of jet velocity are numerically investigated. In the second part, the antisolvent crystallization of two polymorphic forms of L-histidine in the confined impinging jet crystallizer is presented. To the authors' knowledge, this is the most thorough simulation study on impinging jet crystallizers reported to date.

## 2. CFD–Micromixing–Population Balance Model

The development and implementation of the CFD–micromixing–population balance coupled algorithm is presented in detail by Woo et al.,<sup>32</sup> which applied the integrated model to simulate semibatch antisolvent crystallization in a stirred tank. The mathematical details of the models, for application to confined impinging jet crystallization, are presented in this section.

**2.1. Macromixing.** In this work, the macromixing was modeled by the Reynolds-averaged Navier–Stokes (RANS) and transport equations and the  $k$ – $\varepsilon$  turbulence model with enhanced wall treatment<sup>34,35</sup> due to the small volume of the mixing chamber and the confinement of the impinging region by the chamber walls, computed using a commercial CFD software (Fluent 6.2.16, Fluent Inc.). The equations are summarized below; the reader is referred to the software documentation for the nomenclature and more details on the equations.<sup>35,36</sup>

$$\text{continuity equation: } \frac{\partial \rho}{\partial t} + \nabla \cdot (\rho \vec{v}) = 0 \quad (1)$$

$$\text{momentum conservation equation: } \frac{\partial}{\partial t}(\rho \vec{v}) + \nabla \cdot (\rho \vec{v} \vec{v}) = -\nabla p + \nabla \cdot (\bar{\tau}) + \rho \vec{g} \quad (2)$$

$$\begin{aligned} k\text{-}\varepsilon \text{ equations: } \frac{\partial}{\partial t}(\rho k) + \nabla \cdot (\rho k \vec{v}) = \\ \nabla \cdot \left[ \left( \mu + \frac{\mu_t}{\sigma_k} \right) \nabla \cdot k \right] + G_k - \rho \varepsilon, \quad \frac{\partial}{\partial t}(\rho \varepsilon) + \nabla \cdot (\rho \varepsilon \vec{v}) = \\ \nabla \cdot \left[ \left( \mu + \frac{\mu_t}{\sigma_\varepsilon} \right) \nabla \cdot \varepsilon \right] + C_{1\varepsilon} \frac{\varepsilon}{k} G_k - C_{2\varepsilon} \rho \frac{\varepsilon^2}{k} \end{aligned} \quad (3)$$

where  $\mu_t = \rho C_\mu k^2 / \varepsilon$

$$\text{scalar transport equation: } \frac{\partial}{\partial t}(\rho \varphi_k) + \nabla \cdot (\rho \vec{v} \varphi_k - \rho D_m + D_t) \nabla \cdot \varphi_k = S_{\varphi_k} \quad (4)$$

where  $D_t = \mu_t / \rho Sc_t$ .

The choice of the  $k$ – $\varepsilon$  turbulence model with enhanced wall treatment is based on the analysis presented by Liu and Fox<sup>30</sup> and Gavi et al.<sup>31</sup> Besides the good agreement with the experimental results in Johnson and Prud'homme,<sup>22</sup> Gavi et al.<sup>31</sup> showed that the flow field prediction obtained with RANS using the  $k$ – $\varepsilon$  turbulence model with enhanced wall treatment agreed reasonably well with large eddy simulation (LES) results.

**Table 1. Micromixing Terms for Equations 5 and 6<sup>37</sup>**

model variables	$\mathbf{G}, \mathbf{M}^n$	$\mathbf{G}_s, \mathbf{M}_s^n$
$p_1$	$-\gamma p_1(1 - p_1)$	$\gamma_s p_3$
$p_2$	$-\gamma p_2(1 - p_2)$	$\gamma_s p_3$
$p_3$	$\gamma[p_1(1 - p_1) + p_2(1 - p_2)]$	$-2\gamma_s p_3$
$\langle \mathbf{s} \rangle_3$	$\gamma[p_1(1 - p_1)\langle \phi \rangle_1 + p_2(1 - p_2)\langle \phi \rangle_2]$	$-\gamma_s p_3(\langle \phi \rangle_1 + \langle \phi \rangle_2)$
	$\gamma = [\varepsilon_\xi / (p_1(1 - p_1)(1 - \langle \xi \rangle_3)^2 + p_2(1 - p_2)\langle \xi \rangle_3^2)]$	
	$\gamma_s = [2D_t / (1 - \langle \xi \rangle_3)^2 + \langle \xi \rangle_3^2] \times [\partial \langle \xi \rangle_3 / \partial x_i][\partial \langle \xi \rangle_3 / \partial x_i]$	
	$\langle \xi^2 \rangle = p_1(1 - p_1) - 2p_1 p_3 \langle \xi \rangle_3 + p_3(1 - p_3)\langle \xi \rangle_3^2$	

**2.2. Micromixing.** Micromixing (mixing at a molecular level) was modeled by a three-environment ( $N = 3$ ) presumed-probability density function (PDF) micromixing model, which approximates the fluctuations of the species concentrations on the subgrid scale.<sup>37</sup> One inlet stream (saturated solution) is represented by Environment 1, and the other inlet stream (antisolvent) is represented by Environment 2. Environments 1 and 2 transfer matter by engulfment into Environment 3, where crystallization occurs in a supersaturated solution.<sup>33</sup> The equations, which are coupled with the CFD algorithm,<sup>32</sup> are

$$\frac{\partial \mathbf{p}}{\partial t} + \nabla \cdot (\vec{v} \mathbf{p} - D_t \nabla \cdot \mathbf{p}) = \mathbf{G} + \mathbf{G}_s \quad (5)$$

$$\frac{\partial \langle \mathbf{s} \rangle_n}{\partial t} + \nabla \cdot (\vec{v} \langle \mathbf{s} \rangle_n - D_t \nabla \cdot \langle \mathbf{s} \rangle_n) = \mathbf{M}^n + \mathbf{M}_s^n + p_n \mathbf{S}^n \quad (6)$$

$$\langle \mathbf{s} \rangle_n \equiv p_n \langle \varphi \rangle_n \quad (7)$$

$$\langle \mathbf{s} \rangle \equiv \sum_{n=1}^N p_n \langle \varphi \rangle_n \quad (8)$$

where  $\mathbf{p}$  is the volume fraction vector,  $\langle \mathbf{s} \rangle$  is the overall mean composition,  $\langle \mathbf{s} \rangle_n$  is the weighted composition vector, and  $\langle \phi \rangle_n$  is its mean composition vector in Environment  $n$ , and  $\langle \phi \rangle_1$  and  $\langle \phi \rangle_2$  are given by the compositions in the respective inlet streams. The transport equation for the mixture fraction in Environment 3,  $\langle \xi \rangle_3$ , is also represented by eq 6, and the mean mixture fraction  $\langle \xi \rangle$  is given by eq 8 with  $\langle \xi \rangle_1 = 1$  and  $\langle \xi \rangle_2 = 0$ . The micromixing terms,  $\mathbf{M}^n$  and  $\mathbf{M}_s^n$ , in the right-hand side of the equations are given in Table 1 and  $\mathbf{S}^n$  is the source term (e.g., reaction, crystallization) for the scalars, which is a function of  $\langle \phi \rangle_n$ .

The scalar dissipation rate is expressed as<sup>33</sup>

$$\varepsilon_\xi = C_\varphi \langle \xi^2 \rangle \frac{\varepsilon}{k} \quad (9)$$

As shown by Liu and Fox,<sup>30</sup> the flow field for the confined impinging jets includes regions of low and high turbulence. Therefore, the dependence of the micromixing parameter  $C_\varphi$  on the local turbulent Reynolds number  $Re_l$  was included:

$$C_\varphi = \sum_{n=0}^6 a_n (\lg Re_l)^n \text{ for } Re_l = \frac{k}{\nu \varepsilon} \geq 0.2 \quad (10)$$

where  $\nu$  is the kinematic viscosity, and  $a_0 = 0.4903$ ,  $a_1 = 0.6015$ ,  $a_2 = 0.5851$ ,  $a_3 = 0.09472$ ,  $a_4 = -0.3903$ ,  $a_5 = 0.1461$ , and  $a_6 = -0.01604$ .

The simulation of reactions in confined impinging jets by Liu and Fox<sup>30</sup> and Gavi et al.<sup>31</sup> used the two-environment DQMOM–IEM approach to approximate the presumed-PDF. Both micromixing models have been used in the simulation of precipitation processes.<sup>33</sup> The three-environment model involves

the solution of a single set of discretized population balance equations (PBE) in one mixed environment, which is described next.

**2.3. Population Balance.** To compute the crystal size distribution in the impinging jet crystallizer, the transport equations in the CFD-micromixing model are coupled to a spatially varying PBE. Since this is discussed in detail by Woo et al.,<sup>32</sup> the approach is only summarized here. The spatially varying population balance equation, discretized along the crystal growth axis using a high-resolution finite-volume method,<sup>38,39</sup> is solved as a set of scalar transport equations in the CFD solver. With  $f_j$  denoting the cell-averaged population density between size  $r_{j-1/2}$  and  $r_{j+1/2}$ , the cell-averaged crystal mass,  $f_{w,j}$ , is written as

$$f_{w,j} = \rho_c k_v \int_{r_{j-1/2}}^{r_{j+1/2}} r^3 f_j dr = \frac{\rho_c k_v f_j}{4} ((r_{j+1/2})^4 - (r_{j-1/2})^4) \quad (11)$$

where  $\rho_c$  is the crystal density and  $k_v$  is the crystal volume shape factor. For the well-micromixed case, the scalar transport equation for  $f_{w,j}$  with size-dependent growth is

$$\frac{d}{dt} f_{w,j} + \nabla \cdot (\bar{v} f_{w,j} - D_t \nabla \cdot f_{w,j}) = \begin{cases} \frac{\rho_c k_v}{4 \Delta r} [(r_{j+1/2})^4 - (r_{j-1/2})^4] \times \left\{ -G_{j+1/2} [f_j + \frac{\Delta r}{2} (f_r)_j] + G_{j-1/2} [f_{j-1} + \frac{\Delta r}{2} (f_r)_{j-1}] + B(j=0) \right\} & \text{for } S > 1 \\ \frac{\rho_c k_v}{4 \Delta r} [(r_{j+1/2})^4 - (r_{j-1/2})^4] \times \left\{ -G_{j+1/2} [f_{j+1} - \frac{\Delta r}{2} (f_r)_{j+1}] + G_{j-1/2} [f_j - \frac{\Delta r}{2} (f_r)_j] \right\} & \text{for } S < 1 \end{cases} \quad (12)$$

where  $(f_r)_j$  is the derivative approximated by the minmod limiter,<sup>38</sup>  $S = c/c^*$  is the supersaturation,  $c$  and  $c^*$  are the solution and saturated concentrations, respectively,  $G$  is the growth or dissolution rate, and  $B$  is the nucleation rate. To include the effects of micromixing, eq 12 is written in the form of eq 6, with the right-hand side of eq 12 inserted into the chemical source term in eq 6. The inlet stream with saturated solution is in Environment 1, the inlet stream with antisolvent is in Environment 2, and Environment 3 is a mixture of supersaturated solution and crystals. The assumption of particles following the fluid streamlines is valid in impinging jets as the particles are very small in these systems.

**2.4. Implementation into CFD Solver.** The macromixing and micromixing models are coupled with the population balance in a commercial CFD solver (Fluent 6.2.16, Fluent Inc.) using user-defined functions as described in Woo et al.<sup>32</sup> Because of the symmetry of the geometry, only half the confined impinging jet was modeled and the numerical grid was generated using Gambit 2.2.30 (Fluent Inc.). The geometry and dimensions of the confined impinging jet is shown in Figure 1. Following the work of Liu and Fox<sup>30</sup> and Gavi et al.,<sup>31</sup> the fluid is treated as having constant density and viscosity which were calculated based on mixing the solvents of both inlet streams. This reduced the simulation time while producing negligible effects on the results. For inlet velocities with laminar flow in the inlet pipes (jet Reynolds Number < 2000), the inlet pipe region was specified as a laminar zone.<sup>35</sup> However, the exact nature of the flow in the inlet pipes has to be validated experimentally or with direct numerical simulations since the downstream of the inlet pipes is the impinging jet chamber. The steady-state flow field was first calculated, followed by the time-dependent

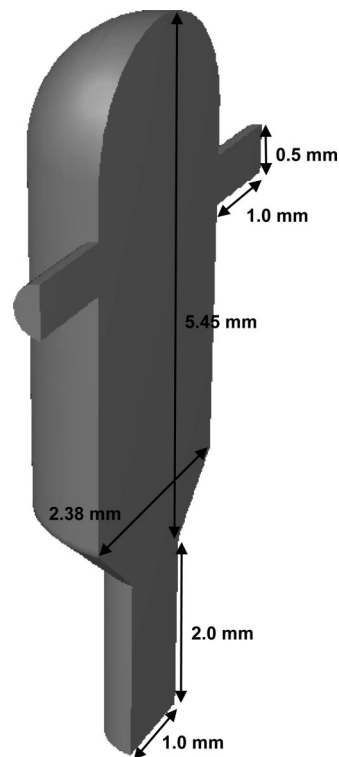


**Figure 1.** Geometry and dimensions for confined impinging jet used for antisolvent crystallization simulations.

computation of the transport eqs 5, 6, and 12 until steady state. Simulations were carried out for jet Reynolds number  $Re_j$  in the range of 200 to 1000. All computations were carried in parallel, across four to eight CPUs, on Xeon 3.06 and 3.2 GHz Linux clusters.

### 3. Confined Impinging Jet Crystallization of Lovastatin

The crystallization of lovastatin from a methanol–water mixture was studied (water is the antisolvent). The solubility data were provided by Merck & Co., Inc. (Rahway, NJ):

$$c^* \text{ at } 23^\circ\text{C (g/kg of solvents)} = \begin{cases} -541V^3 + 534V^2 - 207V + 33.1 & \text{for } V \leq 0.4 \\ -1.62V + 1.62 & \text{for } V > 0.4 \end{cases} \quad (13)$$

where  $V$  is the volume fraction of antisolvent in the solvents. The primary nucleation and growth kinetics are given in Mahajan and Kirwan:<sup>40</sup>

$$B = B_{\text{homogeneous}} + B_{\text{heterogeneous}} \\ B_{\text{homogeneous}} \text{ at } 23^\circ\text{C (\#/s-m}^3\text{)} = 6.97 \times 10^{14} \exp\left(\frac{-15.8}{[\ln S]^2}\right) \\ B_{\text{heterogeneous}} \text{ at } 23^\circ\text{C (\#/s-m}^3\text{)} = 2.18 \times 10^8 \exp\left(\frac{-0.994}{[\ln S]^2}\right) \quad (14)$$

$$G \text{ at } 23^\circ\text{C (m/s)} = 8.33 \times 10^{-30} (2.46 \times 10^3 \ln S)^{6.7} \quad (15)$$

Mahajan and Kirwan<sup>40</sup> indicate that crystal growth for this system is surface integration limited, and the growth rate is size-independent. Secondary nucleation can be neglected due to the small solids density in impinging jets.



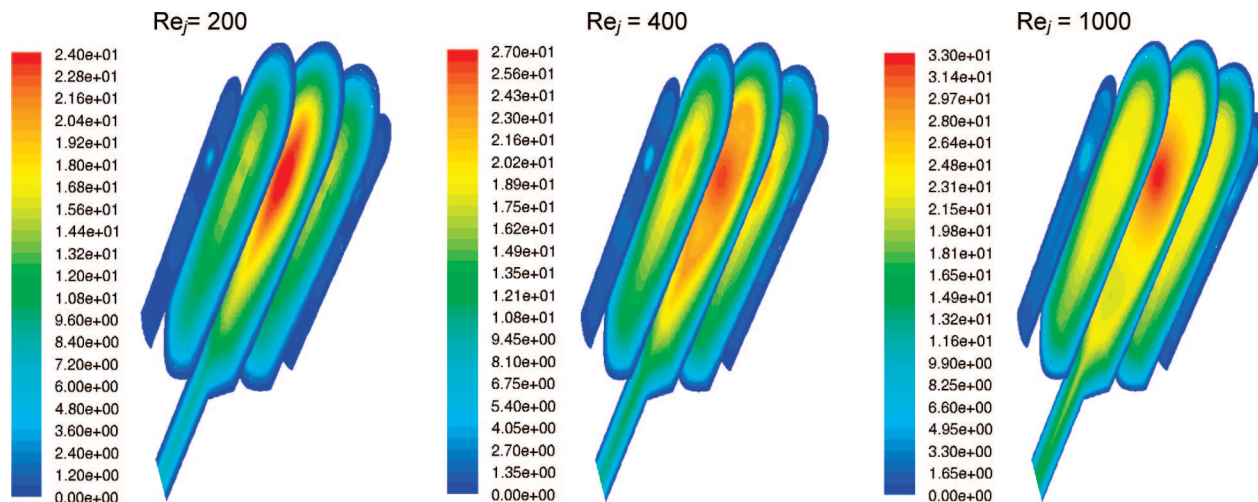


**Figure 2.** Local turbulent Reynolds number in confined impinging jets at steady state for different jet Reynolds numbers.

The simulations were carried out with methanol solution saturated with lovastatin (Environment 1) in one inlet and water (Environment 2) in the other inlet, with an average density of  $891.6 \text{ kg/m}^3$  and viscosity of  $8.0336 \times 10^{-4} \text{ Pa}\cdot\text{s}$ . The density of lovastatin is  $1273 \text{ kg/m}^3$  and the volume shape factor is  $0.000625$ . The PBE was discretized into 30 bins, with  $\Delta r = 8 \text{ }\mu\text{m}$ , for the longest growth axis. The use of effective viscosity, as described in Woo et al.,<sup>32</sup> was omitted because the solid fraction was too small to significantly affect the effective viscosity.

**3.1. Mixing.** The local turbulent Reynolds number field in the confined impinging jets (see Figure 2) agrees well with the simulation results of Liu and Fox.<sup>30</sup> The effects of the jet Reynolds number  $Re_j$  on macromixing and micromixing have been discussed in detail by Liu and Fox<sup>30</sup> and Gavi et al.<sup>31</sup> This section briefly discusses the mixing effects in confined impinging jets on the basis of the three-environment micromixing model.

Other than the region where the liquid jets enter the chamber, the mean mixture fraction  $\langle \xi \rangle$  approaches the value of 0.5 in the confined impinging jets (Figure 3), indicating that macromixing is effective for these jet Reynolds numbers. At a higher jet Reynolds number, each fluid starts to become mixed at a closer distance to the corresponding inlet and the gradient of the mean mixture fraction at the impingement plane is sharper which is consistent with the higher jet momentum. The extent of micromixing near the exit is high but not complete for these inlet velocities ( $p_3 < 1$  in Figure 4). As expected, more micromixing (larger values of  $p_3$ ) is achieved at a higher jet Reynolds number due to higher turbulence (see Figure 2) which results in faster engulfment and micromixing rates.

Since crystallization only occurs in the mixed Environment 3, we are interested in the proportions of the inlet streams in Environment 3, which affects the local supersaturation and crystallization rates, and thus the crystal size distribution. At higher jet Reynolds number, the faster engulfment into Environment 3 (Figure 4) is associated with its mixture fraction  $\langle \xi \rangle_3$  on the two sides of the impingement plane containing more fluid from the inlets (see Figure 5). Toward the outlet, the composition becomes nearly uniform ( $\langle \xi \rangle_3 \rightarrow 0.5$ ). Only the mean compositions, but not the mixture fraction nor compositions in the individual environments, have been presented in the earlier simulation work on confined impinging jets,<sup>30,31</sup> while the latter impacts the local crystallization rates.

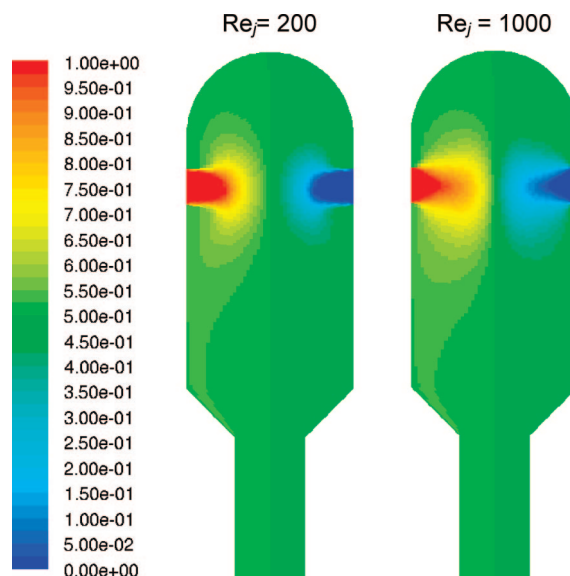


**Figure 3.** Mean mixture fraction  $\langle \xi \rangle$  along the symmetry plane of the mixing chamber of the confined impinging jets at steady state (left inlet: methanol saturated with lovastatin, right inlet: water).

**3.2. Crystallization Dynamics.** Figure 6 shows steady-state spatial distributions for the mixed Environment 3, where crystallization occurs. The solute concentration is analogous to the mixture fraction, since the mixture fraction describes the proportion of fluids from each inlet being mixed. The antisolvent composition plot is nearly a mirror image of the mixture fraction plot, with the antisolvent coming from Environment 2. The saturation concentration in Environment 3 is much higher close to the left inlet where the concentration of antisolvent is lower, due to the cubic behavior of the solubility curve (eq 13). The solute concentration and saturation concentration fields in Figure 6 are associated with nearly uniform supersaturation and local nucleation and growth rates in the mixed Environment 3 for  $Re_j = 200$ , and low supersaturation and crystallization rates close to the left inlet for  $Re_j = 1000$  (see Figure 7). The nearly uniform supersaturation and crystallization rates within Environment 3 do not mean that better mixing occurs at lower jet Reynolds number, as the segregation of the two fluids is much larger and the volume of the mixed Environment 3 is much lower under those conditions (see Figure 4).

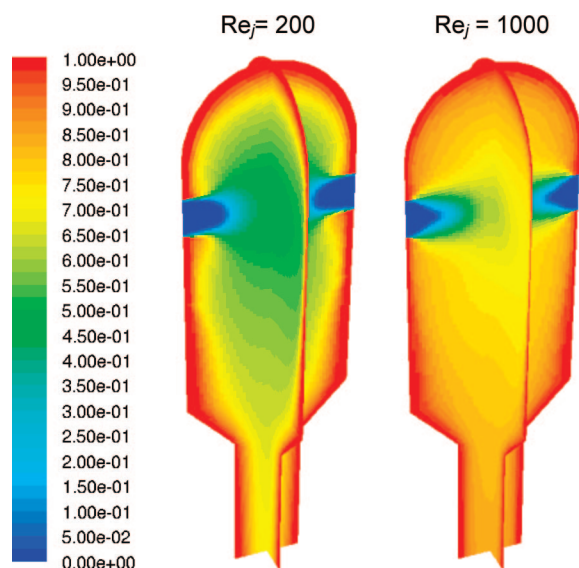


**Figure 4.** Volume fraction of the mixed environment ( $p_3$ ) in the confined impinging jets at steady state (left inlet: methanol saturated with lovastatin, right inlet: water).

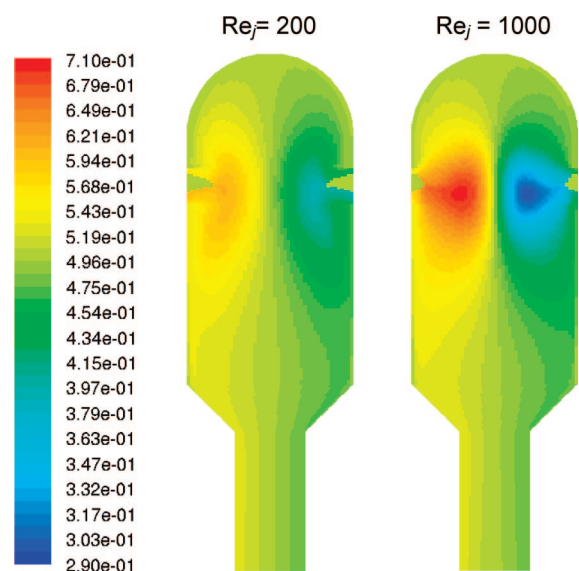


**Figure 5.** Mixture fraction of the mixed environment ( $\langle \xi \rangle_3$ ) along the symmetry plane of the mixing chamber of the confined impinging jets at steady state (left inlet: methanol saturated with lovastatin, right inlet: water).

Table 2 indicates that the spatially averaged supersaturation and crystallization rates in the mixed Environment 3 are  $\sim 2\%$  lower for  $Re_j = 1000$  compared to  $Re_j = 200$ . However, the total volume of the mixed Environment 3 is  $\sim 12\%$  higher for  $Re_j = 1000$ . The higher jet Reynolds number results in more effective mixing for crystallization in confined impinging jets, as the reduced segregation is more than sufficient to compensate for the slight reduction in crystallization rates.

**3.3. Effect of Jet Reynolds Number on Crystal Size Distribution.** Figure 8 shows the crystal size distribution at the outlet of the impinging jet for different jet Reynolds numbers. The monotonically decreasing shape of the crystal size distribution computed from the simulations is very similar to that obtained in the experiments by Mahajan and Kirwan<sup>18</sup> for the same crystallization system for a nonsubmerged unconfined impinging jet.

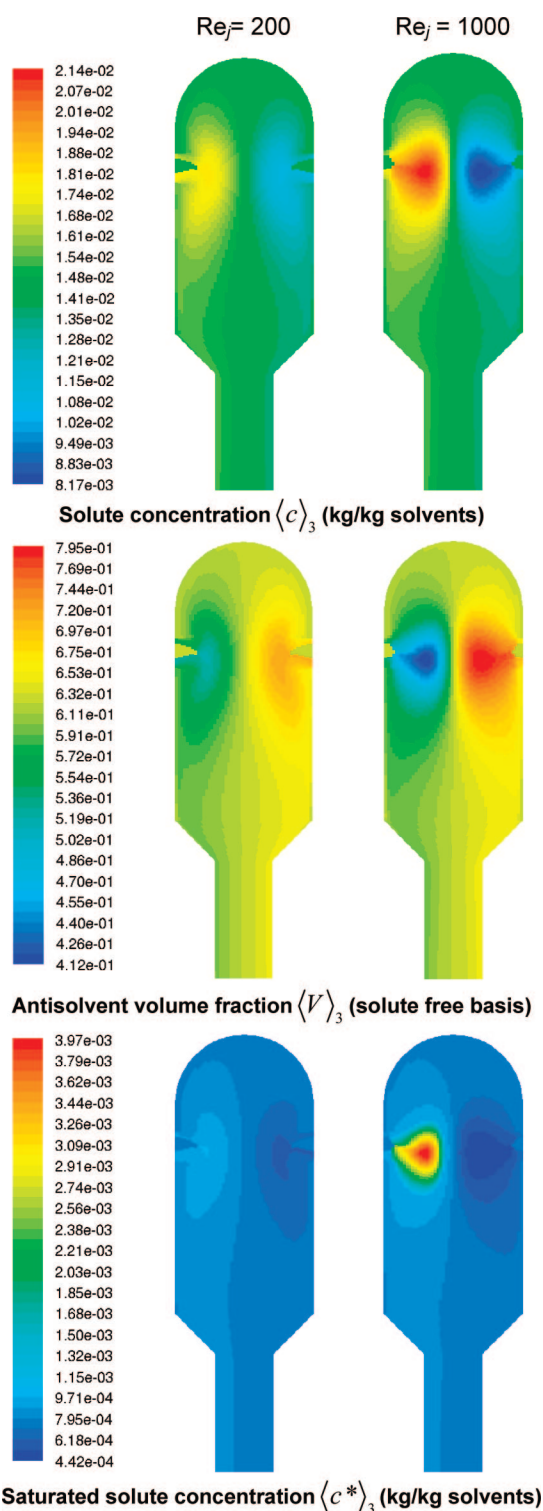


**Figure 6.** Solute concentration, volume fraction of antisolvent, and the corresponding saturated solute concentration in the mixed environment along the symmetry plane of the confined impinging jets at steady-state crystallization of lovastatin (left inlet: methanol saturated with lovastatin, right inlet: water).

The crystal size distribution is much broader with much higher crystal number and mass with reduction in the jet velocity. It is primarily the longer residence time at lower inlet velocity that results in a larger extent of nucleation and growth of crystals at the outlet, since the spatial averages of the nucleation and growth rates over the crystallizer have similar values for different jet Reynolds number (see Table 2). The longer residence time for

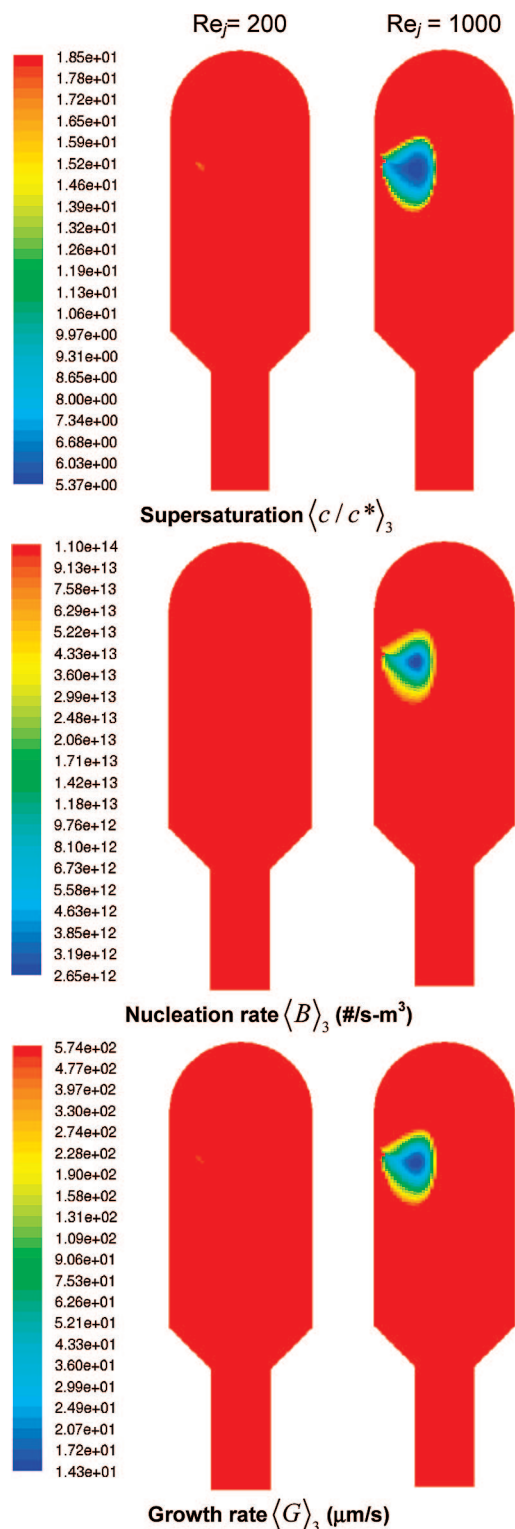


**Figure 7.** Supersaturation, nucleation rates, and growth rates in the mixed environment along the symmetry plane of the confined impinging jets during the steady-state crystallization of lovastatin (left inlet: methanol saturated with lovastatin, right inlet: water).

the lower jet velocities allow more time for crystals to nucleate and grow, hence broadening the crystal size distribution.

The experiments in Mahajan and Kirwan<sup>18</sup> were performed at one residence time for different jet velocities by adjusting the distance of the collection point. Fewer and smaller crystals with a narrower size distribution were obtained for higher jet Reynolds numbers (see Figure 11 of Mahajan and Kirwan<sup>18</sup>).

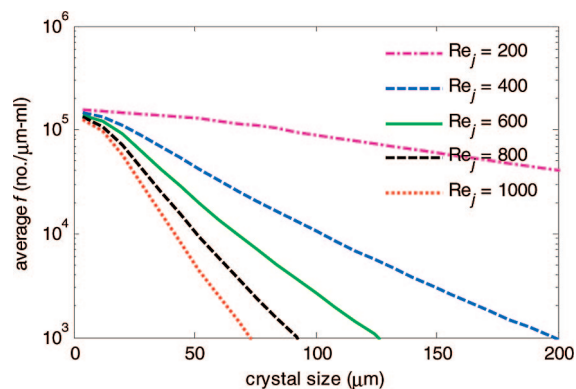


**Figure 8.** Crystal size (longest dimension) distributions of lovastatin obtained from the confined impinging jets at different jet Reynolds numbers.

**Table 2.** Total Volume of Mixed Environment 3 and Spatially Averaged Supersaturation and Crystallization Rates in the Mixed Environment 3 for Different Jet Reynolds Number,  $Re_j$

values in mixed Environment 3	$Re_j = 200$	$Re_j = 1000$
total volume ( $\text{mm}^3$ )	7.55	8.43
average supersaturation	18.5	18.2
average nucleation rate ( $\#/s\text{-m}^3$ )	$1.09 \times 10^{14}$	$1.07 \times 10^{14}$
average growth rate in ( $\mu\text{m/s}$ )	$5.73 \times 10^2$	$5.57 \times 10^2$

The size distribution for the higher jet Reynolds number in the experiments of Mahajan and Kirwan<sup>18</sup> would shift toward fewer and smaller crystals with a narrower distribution if the collection point had not been adjusted to increase the residence time. This would have led to a more pronounced variation of size distribution with jet Reynolds number, which would give the same trend with jet Reynolds number seen in the simulations (see Figure 8).

From the industrial point of view, the simulation predictions in Figure 8 can guide the selection of operations (for example, jet velocity or inlet concentrations) of a confined impinging jet toward a desired crystal size distribution specified by the method of drug administration and its dissolution requirements. Similar plots as Figure 8 could be computed for different three-dimensional geometries for the confined impinging jet (for example, geometries with different amounts of space above the confined jets, or with different diameters for the inlet and outlet pipes), and used to guide the design of the geometry to achieve a particular desired CSD.

#### 4. Polymorphic Crystallization of L-Histidine in a Confined Impinging Jet

The regulatory and drug delivery reasons that necessitate the production of one specific polymorphic form of an active pharmaceutical ingredient are well recognized.<sup>41</sup> The development of a robust and efficient crystallization process to produce crystals of a specific polymorphic form has been considered challenging and, as a minimum, requires a detailed understanding of both the thermodynamics and the crystallization kinetics of the polymorphs for a given system.<sup>42,43</sup> The choice of solvent or solvent composition can affect the formation and the subsequent transformation of polymorphs.<sup>10,44,45</sup> For antisolvent crystallization, the crystallization and subsequent transformation of polymorphs can be affected by initial concentration, addition rate of antisolvent, seeding, and temperature.<sup>43,46–49</sup>

To the authors' knowledge, there are currently no publications on polymorphic crystallization in impinging jets. However, the formation of multiple hydrates of calcium oxalate in an



impinging jet and Y-mixer has been reported by Hacherl et al.<sup>19</sup> and Haselhuhn and Kind,<sup>14</sup> respectively. In this section, the polymorphic crystallization of L-histidine (stable form A and metastable form B) in a water–ethanol mixture in a confined impinging jet, where ethanol is the antisolvent, was simulated with the CFD–micromixing–population balance model. The solubility data and growth kinetics are<sup>50</sup>

$$c_A^* \text{ at } 20^\circ\text{C (mol/L of solvents)} = -1.33V^3 + 1.86V^2 - 1.02V + 0.256 \quad \text{for } V \leq 0.6$$

$$c_B^* \text{ at } 20^\circ\text{C (mol/L of solvents)} = -1.21V^3 + 1.78V^2 - 1.05V + 0.274 \quad \text{for } V \leq 0.6 \quad (16)$$

$$G_j \text{ at } 20^\circ\text{C (m/s)} = k_{g,j} (S_j - 1)^{g_j} \quad \text{for } V \leq 0.4$$

$$k_{g,A} = 3.68 \times 10^{-5} V^2 - 2.90 \times 10^{-5} V + 5.77 \times 10^{-6}$$

$$k_{g,B} = -1.37 \times 10^{-6} V^2 - 2.74 \times 10^{-7} V + 5.37 \times 10^{-7}$$

$$g_A = -47.0V^2 + 16.5V + 3.40$$

$$g_B = -11.4V^2 - 6.91V + 1.40 \quad (17)$$

where  $V$  is the volume fraction of ethanol and  $S_j = c/c_j^*$ . The size independence of these growth kinetics is consistent with the statement of Roelands et al.<sup>51</sup> that crystal growth for this system is limited by the polynuclear growth mechanism. The nucleation kinetics are<sup>51</sup>

$$B_j \text{ at } 20^\circ\text{C (\#/s-m}^3\text{)} = B_{j,\text{heterogeneous}} = 10^{20} \times \exp\left[\frac{-1.19\psi_j}{(\ln S_j)^2} \left(\ln \frac{1}{0.108c_j^*}\right)^3\right] \quad (18)$$

$$\psi_A = 0.3, \psi_B = 0.255$$

Only the primary heterogeneous nucleation kinetic expression was applied as the metastable limit for the homogeneous nucleation was not exceeded in the simulations, and secondary nucleation was neglected due to the very small particle volume in impinging jets. The solvent-mediated transformation kinetics were excluded as the solution was supersaturated for both polymorphs throughout the crystallizer.

The simulation had saturated water solution in one inlet and saturated solution of water and ethanol in a 3:2 volume ratio in the other inlet (the inlet saturated concentration was calculated from the solubility curve of polymorph B). The average density of 956.56 kg/m<sup>3</sup> and viscosity of  $1.0355 \times 10^{-3}$  Pa·s were used to compute the flow field. The density of L-histidine is 1440 kg/m<sup>3</sup> and the volume shape factor is 2/3. The PBE was discretized into 20 bins for both polymorphs, with  $\Delta r = 0.0008$  μm. As in the previous section, the use of effective viscosity was omitted because the solid fraction was too small to significantly affect the effective viscosity.

**4.1. Crystallization Dynamics and Crystal Product Quality.** The supersaturation and nucleation rates and growth rates of form A and B in the mixed Environment 3 for the jet Reynolds number of 1000 are shown in Figure 9. Overall, the supersaturation is lower for the metastable polymorph B since which has higher solubility. The nucleation rates are comparatively higher for polymorph B, while the growth rates are slightly lower. The crystal size distributions at the outlet are shown in Figure 10. Similar to the lovastatin system, the crystal number density of L-histidine polymorphs monotonically decreases with crystal size. The trend for the variation of the crystal size distribution with jet Reynolds number is also consistent with the observations for the lovastatin system. The higher nucleation

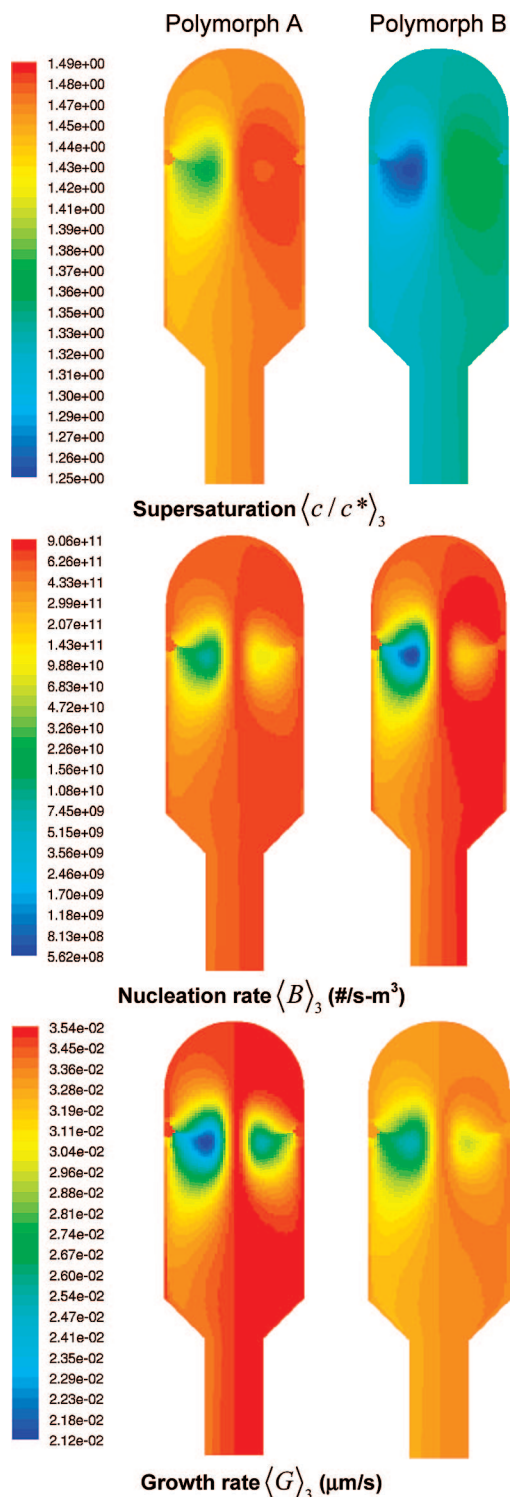


**Figure 9.** Supersaturation, nucleation rates, and growth rates in the mixed environment along the symmetry plane of the confined impinging jets at steady-state crystallization of L-histidine polymorphs for  $Re_j = 1000$  (left inlet: L-histidine saturated in water; right inlet: L-histidine saturated in water and ethanol in a 3:2 volume ratio).

rates for polymorph B result in a slightly larger number of form B crystals at the small sizes, and the higher growth rate for polymorph A results in a slightly larger number of form A crystals at the large sizes.

Ostwald's rule of stages does not apply to this crystallization process since both stable and metastable polymorphs are nucleated simultaneously, which is consistent with the experi-

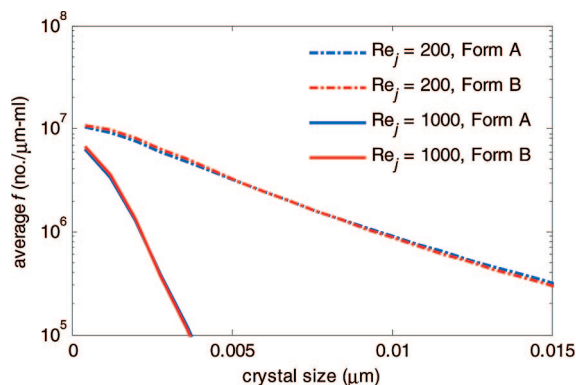


**Figure 10.** Crystal size distributions of polymorphs A and B of L-histidine obtained from the confined impinging jets at different jet Reynolds numbers.

mental data reported by Kitamura et al.<sup>50</sup> and Roelands et al.<sup>51</sup> The crystallization of L-histidine in an average of 20 vol% ethanol that was used in the simulations is an example of concomitant polymorphic crystallization.<sup>52</sup>

This study demonstrates the capability of the CFD–micromixing–population balance algorithm to simulate polymorphic systems. For this concomitant polymorphic system, the polymorph ratio does not vary much with the jet Reynolds velocity ( $\sim 0.5$ ), which makes it possible to tailor the crystal size distribution, by adjusting the inlet velocity, without affecting the relative amounts of polymorph present. This information would be useful for achieving a desired crystal size distribution as well as designing the solvent-mediated transformation process in the subsequent step.<sup>43</sup>

## 5. Conclusions and a Look to the Future

In this paper, the capability of the CFD–micromixing–population balance model in modeling crystallization in confined impinging jets, taking into account the effects of macromixing and micromixing, was demonstrated. For crystallization of lovastatin, the simulation results indicate that more and larger crystals, with wider size distribution, were produced at a lower jet Reynolds number due to a longer residence time for nucleation and growth. Such a trend was also observed experimentally in unconfined impinging jets for the same system.<sup>18</sup> The polymorphic crystallization of L-histidine was also simulated to demonstrate the capability of the CFD–micromixing–population balance model to simulate the crystallization of polymorphic systems.

As future work, experimental systems should be set up to validate the model so that this simulation code can be applied to different systems with confidence. A full validation requires accurate measurements of crystal size distributions and solution concentrations not only at the outlet, but across the entire three-dimensional field in the impinging jet crystallizer. Hence, possible various sensors that are capable of collecting such data should be explored. A complete validation would help to improve the simulation model, and thus advance the technology in industrial crystallization.

The simulations related the crystal size distribution and ratio of polymorphs to changes in the inlet jet velocity. The simulation method enables an investigation into the variation of other operating variables such as the inlet concentrations and design variables such as the 3D geometry of the impinging jet to determine their effects on the crystal size distribution and the ratio of polymorphs. Note that in the initial stages of process

development, the pharmaceutical compound is usually available in very small amounts. This makes it difficult to carry out numerous trial-and-error experiments to determine the operating conditions that give a desired crystal size distribution. Simulation tools could provide a technological advancement to industrial crystallization and process development in the pharmaceutical industry, by making it possible to design impinging jet crystallizers in-silico to give desired crystal size distributions. The development of the crystallization process would be done in the following steps:

(1) For a given antisolvent–solvent–solute crystallization system, hydrodynamics-independent crystallization kinetics would be first determined by using small amounts of the pharmaceutical compound, for example, with the use of microfluidic devices. Many designs for microfluidic devices have been developed to mix fluids in very short times, so that the system is not transport-limited.<sup>53</sup>

(2) With the estimated parameters for the CFD–micromixing–population balance model and crystallization kinetics, the CFD–micromixing–population balance model is used to simulate the crystal size distribution for a wide range of operating conditions (for example, inlet velocities and inlet concentrations). The simulation results then can be used to identify the set of operating conditions that produces the crystal size distribution that meets the bioavailability requirements.

This design strategy would allow an impinging jet crystallizer and its operations to be designed in a systematic engineering manner. In addition, it would reduce the use of pharmaceutical compound to a minimum, and with the availability of faster computers, this process design would be done in shorter times.

**Acknowledgment.** The Institute of Chemical and Engineering Sciences (Singapore) and the National Center of Supercomputing Applications are acknowledged for the computational resources. The authors thank Brian K. Johnson for discussions on confined impinging jets, Louis S. Crocker and Erik A. Dienemann for comments on the manuscript, and Merck & Co., Inc. for providing the solubility of lovastatin. X.Y.W. acknowledges the Singapore Agency for Sciences, Technology and Research for her research scholarship.

## References

- (1) Midler, M.; Paul, E. L.; Whittington, E. F.; Futran, M.; Liu, P. D.; Hsu, J.; Pan, S.-H. U.S. Patent 5,314,506, 1994.
- (2) D'Aquino, R. *CEP Mag.* **2004**, *100*, 7–14.
- (3) am Ende, D. J.; Crawford, T. C.; Weston, N. P. U.S. Patent 6,558,435, 2003.
- (4) Dauer, R.; Mokrauer, J. E.; McKeel, W. J. U.S. Patent 5,578,279, 1996.
- (5) Lindrud, M. D.; Kim, S.; Wei, C. U.S. Patent 6,302,958, 2001.
- (6) am Ende, D. J.; Brenek, S. J. *Am. Pharm. Rev.* **2004**, *7*, 98–104.
- (7) Bauer-Brandl, A. *Int. J. Pharm.* **1996**, *140*, 195.
- (8) Bauer-Brandl, A. *Int. J. Pharm.* **1996**, *145*, 253.
- (9) Leung, S. S.; Padden, B. E.; Munson, E. J.; Grant, D. J. W. *J. Pharm. Sci.* **1998**, *87*, 501–507.
- (10) Shekunov, B. Y.; York, P. *J. Cryst. Growth.* **2000**, *211*, 122–136.
- (11) Nagao, L. M.; Lyapustina, S.; Munos, M. K.; Capizzi, M. D. *Cryst. Growth Des.* **2005**, *5*, 2261–2267.
- (12) Taylor, K. In *Pharmaceutics*; 2nd ed.; Aulton, M. E., Ed.; Churchill Livingstone: Spain, 2002; pp 473–488.
- (13) Choi, Y. J.; Chung, S. T.; Oh, M.; Kim, H. S. *Cryst. Growth Des.* **2005**, *5*, 959–968.
- (14) Haselshuhn, F.; Kind, M. *Chem. Eng. Technol.* **2003**, *26*, 347–353.
- (15) Schwarzer, H. C.; Peukert, W. *AIChE J.* **2004**, *50*, 3234–3247.
- (16) Schwarzer, H. C.; Schwertfirm, F.; Manhart, M.; Schmid, H. J.; Peukert, W. *Chem. Eng. Sci.* **2006**, *61*, 167–181.
- (17) Stahl, M.; Alund, B. L.; Rasmuson, A. C. *AIChE J.* **2001**, *47*, 1544–1560.
- (18) Mahajan, A. J.; Kirwan, D. J. *AIChE J.* **1996**, *42*, 1801–1814.



- (19) Hacherl, J. M.; Paul, E. L.; Buettner, H. M. *AIChE J.* **2003**, *49*, 2352–2362.
- (20) Johnson, B. K.; Prud'homme, R. K. *Aust. J. Chem.* **2003**, *56*, 1021–1024.
- (21) Marchisio, D. L.; Rivautella, L.; Barresi, A. A. *AIChE J.* **2006**, *52*, 1877–1887.
- (22) Johnson, B. K.; Prud'homme, R. K. *AIChE J.* **2003**, *49*, 2264–2282.
- (23) Stan, G.; Johnson, D. A. *AIAA J.* **2001**, *39*, 1901–1908.
- (24) Unger, D. R.; Muzzio, F. J. *AIChE J.* **1999**, *45*, 2477–2486.
- (25) Zhao, Y.; Brodkey, R. S. *Can. J. Chem. Eng.* **1998**, *76*, 536–545.
- (26) Teixeira, A. M.; Santos, R. J.; Rui, M.; Costa, P. F. N.; Lopes, J. C. B. *AIChE J.* **2005**, *51*, 1608–1619.
- (27) Kusch, H. A.; Ottino, J. M.; Shannon, D. M. *Ind. Eng. Chem. Res.* **1989**, *28*, 302–315.
- (28) Santos, R. J.; Teixeira, A. M.; Lopes, J. C. B. *Chem. Eng. Sci.* **2005**, *60*, 2381–2398.
- (29) Sohrabi, M.; Marvast, M. A. *Ind. Eng. Chem. Res.* **2000**, *39*, 1903–1910.
- (30) Liu, Y.; Fox, R. O. *AIChE J.* **2006**, *52*, 731–744.
- (31) Gavi, E.; Marchisio, D. L.; Barresi, A. A. *Chem. Eng. Sci.* **2007**, *62*, 2228–2241.
- (32) Woo, X. Y.; Tan, R. B. H.; Chow, P. S.; Braatz, R. D. *Cryst. Growth Des.* **2006**, *6*, 1291–1303.
- (33) Wang, L. G.; Fox, R. O. *AIChE J.* **2004**, *50*, 2217–2232.
- (34) Pope, S. B. *Turbulent Flows*; Cambridge University Press: Cambridge, U. K., 2000.
- (35) *Fluent 6.2 User's Guide*; Fluent Inc.: Lebanon, NH, 2005.
- (36) *Fluent 6.2 UDF Manual*; Fluent Inc.: Lebanon, NH, 2005.
- (37) Fox, R. O. *Computational Models for Turbulent Reacting Flows*; Cambridge University Press: Cambridge, U. K., 2003.
- (38) Kurganov, A.; Tadmor, E. *J. Comput. Phys.* **2000**, *160*, 241–282.
- (39) Leveque, R. J. *Finite Volume Methods for Hyperbolic Problems*; Cambridge University Press: Cambridge, U. K., 2002.
- (40) Mahajan, A. J.; Kirwan, D. J. *J. Cryst. Growth.* **1994**, *144*, 281–290.
- (41) Chemburkar, S. R.; Bauer, J.; Deming, K.; Spiwek, H.; Patel, K.; Morris, J.; Henry, R.; Spanton, S.; Dziki, W.; Porter, W.; Quick, J.; Bauer, P.; Donaubaue, J.; Narayanan, B. A.; Soldani, M.; Riley, D.; McFarland, K. *Org. Process Res. Dev.* **2000**, *4*, 413–417.
- (42) Muller, M.; Meier, U.; Wieckhusen, D.; Beck, R.; Pfeffer-Hennig, S.; Schneeberger, R. *Cryst. Growth Des.* **2006**, *6*, 946–954.
- (43) Kitamura, M. *Cryst. Growth Des.* **2004**, *4*, 1153–1159.
- (44) Khoshkoo, S.; Anwar, J. *J. Phys. D: Appl. Phys.* **1993**, *26*, B90–B93.
- (45) Wang, J.; Loose, C.; Baxter, J.; Cai, D. W.; Wang, Y. L.; Tom, J.; Lepore, J. *J. Cryst. Growth.* **2005**, *283*, 469–478.
- (46) Kitamura, M.; Nakamura, K. *J. Chem. Eng. Jpn.* **2002**, *35*, 1116–1122.
- (47) Kitamura, M.; Hironaka, S. *Cryst. Growth Des.* **2006**.
- (48) Kitamura, M.; Sugimoto, M. *J. Cryst. Growth.* **2003**, *257*, 177–184.
- (49) Toth, J.; Kardos-Fodor, A.; Halasz-Peterfi, S. *Chem. Eng. Process.* **2005**, *44*, 193–200.
- (50) Kitamura, M.; Furukawa, H.; Asaeda, M. *J. Cryst. Growth.* **1994**, *141*, 193–199.
- (51) Roelands, C. P. M.; Jiang, S.; Kitamura, M.; ter Horst, J. H.; Kramer, H. J. M.; Jansens, P. *J. Cryst. Growth Des.* **2006**, *6*, 955–963.
- (52) Bernstein, J.; Davey, R. J.; Henck, J. O. *Angew. Chem., Int. Ed.* **1999**, *38*, 3441–3461.
- (53) Squires, T. M.; Quake, S. R. *Rev. Mod. Phys.* **2005**, *77*, 977–1026.

CG800095Z